

Cite this: *Nanoscale*, 2020, **12**, 10051

Enzyme-assisted mineralization of calcium phosphate: exploring confinement for the design of highly crystalline nano-objects†

E. Colaço,^a D. Lefèvre,^b E. Maisonhaute,^c D. Brouri,^d C. Guibert,^d
C. Dupont-Gillain,^b K. El Kirat,^a S. Demoustier-Champagne^b and
J. Landoulsi^{*,a,d}

In hard tissues of vertebrates, calcium phosphate (CaP) biomineralization is a fascinating process that combines specific physicochemical and biochemical reactions, resulting in the formation of extracellular matrices with elegant nanoarchitectures. Although several “biomimetic” strategies have been developed for the design of mineralized nanostructured biointerfaces, the control of the crystallization process remains complex. Herein, we report an innovative approach to overcome this challenge by generating, *in situ*, CaP precursors in a confined medium. For this purpose, we explore a combination of (i) the layer-by-layer assembly, (ii) the template-based method and (iii) the heterogeneous enzymatic catalysis. We show the possibility of embedding active alkaline phosphatase in a nanostructured multilayered film and inducing the nucleation and growth of CaP compounds under different conditions. Importantly, we demonstrate that the modulation of the crystal phase from spheroid-shaped amorphous CaP to crystalline platelet-shaped hydroxyapatite depends on the degree of confinement of active enzymes. This leads to the synthesis of highly anisotropic mineralized nanostructures that are mechanically stable and with controlled dimensions, composition and crystal phase. The present study provides a straightforward, yet powerful, way to design anisotropic nanostructured materials, including a self-supported framework, which may be used in broad biomedical applications.

Received 26th February 2020,

Accepted 15th April 2020

DOI: 10.1039/d0nr01638a

rsc.li/nanoscale

1. Introduction

The design of anisotropic nano-objects, such as nanotubes and nanowires, has attracted growing interest in biomedical research owing to their fine-tuned physical and chemical properties. In particular, nanotubes incorporating bioactive molecules are especially interesting and have several advantages relative to spherical nanoparticles that are typically used in biotechnological applications, such as drug delivery nano-carriers or nano-bioreactors.^{1–5} Firstly, nanotubes offer more possibilities of tailoring the functionality of the nanostructure

than nanospheres. They have indeed distinct outer and inner surfaces, which can be differentially (bio)-chemically functionalized. This opens the possibility, for instance, of loading the inside of a nanotube with a specific biochemical payload while imparting chemical features to the outer surface that renders it biocompatible. Secondly, nanotubes have a larger inner volume than nanospheres of the same diameter, which can be filled with any desired (bio)-chemical species ranging in size from small molecules to large macromolecules, such as proteins. Thirdly, cylindrical nanotubes possess open mouths, which make the inner surface accessible and allow the incorporation or release of species into or from the tubes, particularly easy. Finally, recent reports have suggested that the use of anisotropic geometry with higher aspect ratio would increase the chances of cell internalization.⁵ A combination of the template-based synthesis and the layer-by-layer (LbL) assembly method has been proposed as a powerful technique for the elaboration of nano-objects with highly regular dimensions.⁶ The use of track-etched polymer membranes⁷ is, indeed, an efficient way to produce monodisperse objects with a high aspect ratio: their diameter is defined by the nanopore size (from 30 nm up to a few μm) and their length by the template

^aLaboratoire de Biomécanique & Bioingénierie, CNRS, Université de Technologie de Compiègne, BP 20529 F-60205 Compiègne Cedex, France

^bInstitute of Condensed Matter and Nanosciences, Bio & Soft Matter, Université catholique de Louvain, Croix du Sud 1 (L7.04.02), 1348 Louvain-la-Neuve, Belgium.

E-mail: sophie.demoustier@uclouvain.be

^cSorbonne Université, CNRS, Laboratoire Interfaces et Systèmes Electrochimiques, LISE, F-75005 Paris, France

^dSorbonne Université, CNRS, Laboratoire de Réactivité de Surface, LRS, F-75005 Paris, France. E-mail: jesse.landoulsi@sorbonne-universite.fr

† Electronic supplementary information (ESI) available. See DOI: 10.1039/d0nr01638a

thickness (from 5 to 25 μm). The LbL technique offers the possibility to incorporate a variety of (macro)molecules of biological interest, as previously demonstrated for globular⁸ and fibrillar proteins,^{9,10} enzymes,^{11,12} biomembrane fractions,¹³ virus,¹⁴ *etc.* (for recent review see ref. 15). Moreover, it is a versatile technique which may be applied to almost all substrates independently of their shape, chemical composition and physical properties, including nanoporous materials.¹⁶

Bioactive nanotubes/nanowires have been obtained by some of us^{17–19} and other groups.^{20–22} They were successfully used for different purposes, such as the control of preosteoblast adhesion.¹⁸ These functional anisotropic nano-objects are indeed relevant for the design of nanostructured biointerfaces mimicking the extracellular matrix (ECM). Their dimensions, high surface area/volume ratio, and biocompatibility resemble those of natural ECM fibers. In many situations of practical relevance, nanotubes exhibit poor mechanical stability when used in a biological medium. This requires their strengthening, which may be achieved by reinforcing the nanotube walls by incorporating rigid compounds, such as polypyrrol,^{23,24} or inorganic nanoparticles, however with a possible consequence on the chemical composition of the final nano-objects.

In connective tissues, the ECM of which is composed of the mineral phase, such as bone, the design of these nano-objects is particularly relevant for the control of cell–material interaction. In addition to the mechanical stability, the control of the chemical composition of the mineral phase, typical calcium phosphate (CaP), is crucial to direct the cell behavior.^{25–27} The crystallinity of CaP compounds is also a key parameter to be considered when the mineral is in contact with cells (*e.g.* in implants). This may influence the remodeling process, due to the different dissolution rates of the CaP

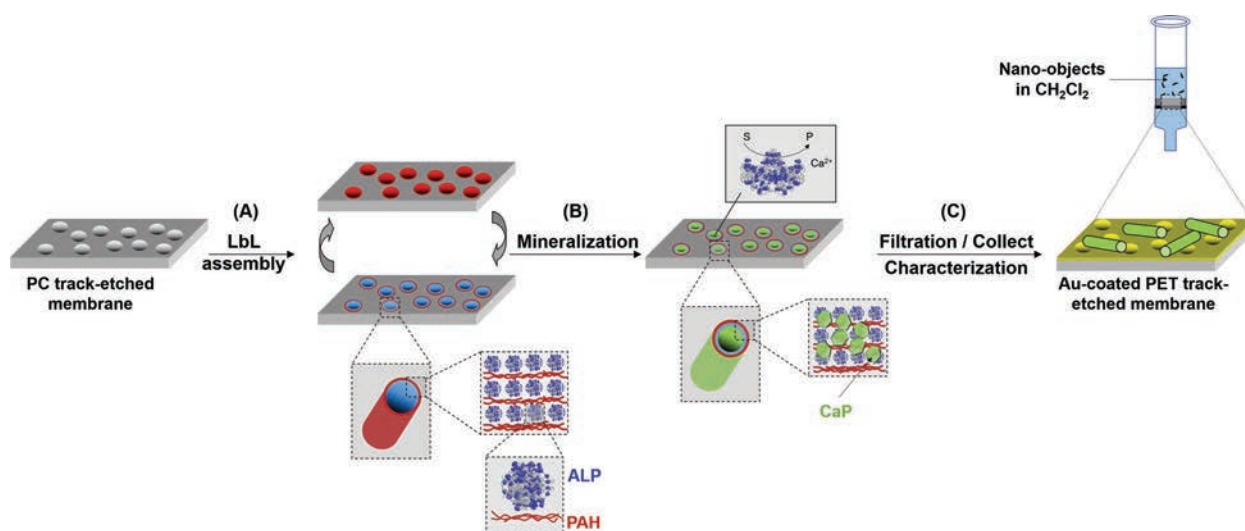
phases, and may directly impact cell adhesion, proliferation and differentiation.²⁸

In vivo, the biogenic crystallization of hydroxyapatite, the main CaP phase in bone, is an outstanding process that requires the combination of specific physicochemical conditions and (bio)chemical reactions, resulting in the formation of highly regular nano-objects with anisotropic features.²⁹ The precise mechanisms of nucleation and growth of CaP remain largely unexplained, particularly in the early stages, but the involvement of extracellular matrix vesicles through an enzyme-assisted process is now well established.³⁰ Particularly, the non-specific alkaline phosphatase (ALP, EC.3.1.3.1) is implicated to generate a CaP precursor, namely orthophosphate ions, as follows:



The concept of enzyme-assisted mineralization has thus motivated the design of CaP-based materials, the control of their crystallinity being the most important challenge.^{31–36}

Following a biomimetic bottom-up approach, we propose, in this study, an innovative strategy to generate mineralized anisotropic nanostructures while tuning their chemical composition and crystal phase. For this purpose, we explore the mechanism by which organisms direct CaP crystallization through a combination of key factors: (i) chemical environment (polyelectrolyte multilayers), (ii) *in situ* generation of CaP precursors (through an enzyme-catalyzed reaction), and (iii) confinement (in a nanoporous template). Relying on the versatile LbL assembly method, we incorporated ALP into a multilayered film within the nanopores of a track-etched membrane (Scheme 1), and explored its activity to generate, *in situ*, orthophosphate ions, thus initiating CaP



Scheme 1 Strategy used for the elaboration and characterization of the mineralized anisotropic nano-objects. (A) Sequential layer-by-layer assembly of (PAH/ALP)_n multilayers. (B) Mineralization by incubation in aqueous solution containing Ca²⁺ ions and α-glycerol phosphate (S), substrate of the enzyme that is converted into phosphate (P, product of the enzymatic reaction), resulting in the formation of calcium phosphate (CaP) mineral. (C) Dissolution of the PC template and collection of the obtained nano-objects by filtration through a Au-coated PET membrane.

mineralization in confinement. Recently, we have used this enzyme in the homogeneous phase and revealed the impact of its catalytic activity on the process of CaP crystallization.³⁷ The building of the enzyme-based multilayers and the mechanism of mineralization are first investigated on flat substrates under different physicochemical conditions, and then monitored *in situ* using a quartz crystal microbalance with dissipation monitoring (QCM-D). The assembly and subsequent mineralization are then performed within nanoporous track-etched membranes. The obtained mineralized nanostructures are characterized, by a variety of techniques, in terms of

morphology, composition, crystallinity and mechanical stability.

2. Results and discussion

2.1 The properties of ALP in aqueous solutions

The isoform of ALP used in this study consists of a multimeric metalloenzyme.³⁸ Fig. 1A presents the change in the hydrodynamic diameter (d_H) and ζ -potential of the enzyme as a function of pH in water. It showed a dependence of the surface charge of the enzyme on pH, as expected, yielding an isoelectric point (iep) near pH = 5.0. This is consistent with theoretical considerations, as the isoelectric point computed using the amino acid composition of the enzyme on the basis of the ProtParam tool is found to be 5.7.³⁹ The hydrodynamic diameter was around 20 nm at pH 7.4 and remained almost unchanged at pH values higher than 6. There was a significant increase in

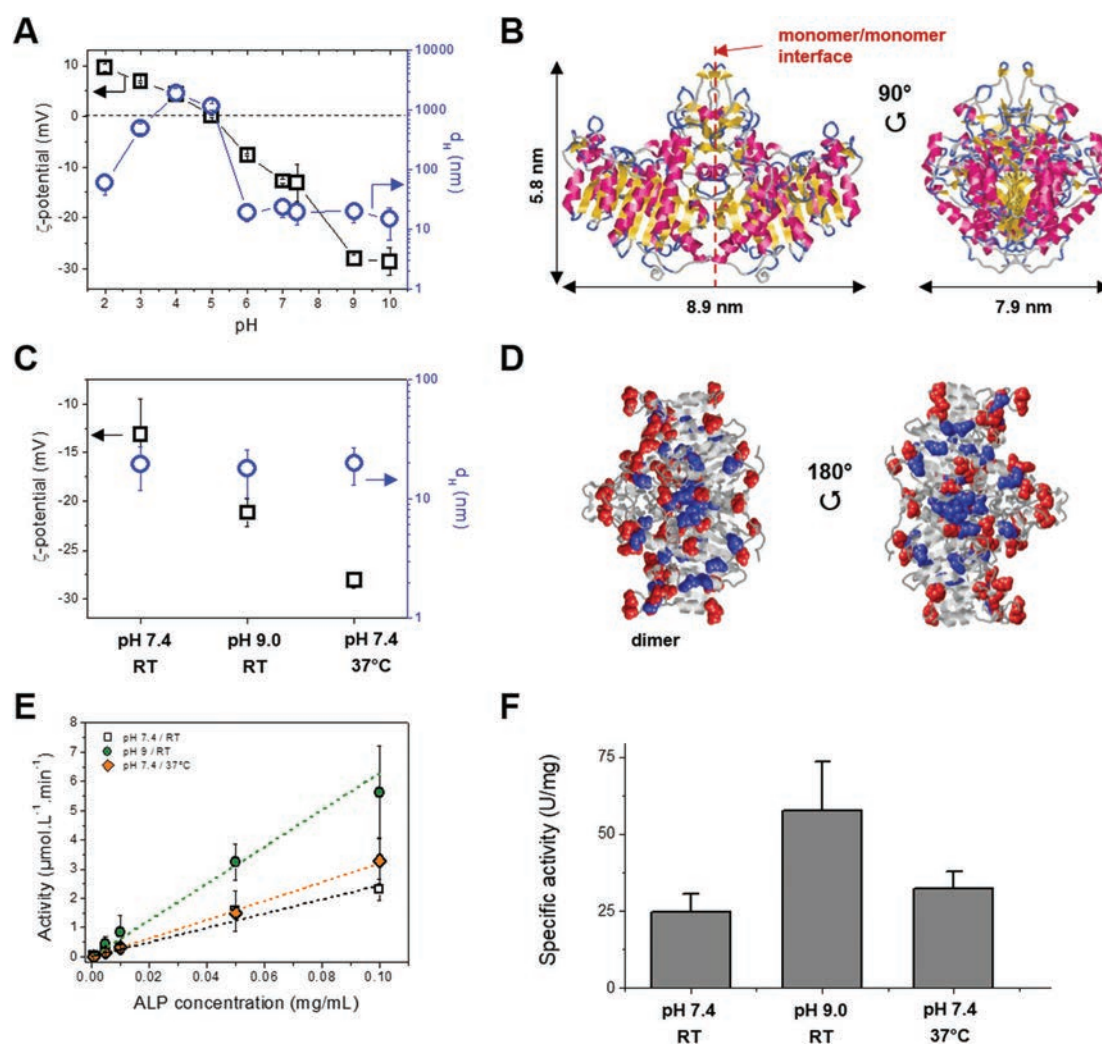


Fig. 1 (A and C) Evolution of ζ -potential (squares) and hydrodynamic diameter (d_H , circles) of ALP (ζ -potential: 0.1 mg mL⁻¹ and DLS: 1.0 mg mL⁻¹) (A) as a function of pH at RT and (C) under different physicochemical conditions: at pH 7.4 (RT), at pH 9 (RT) and at pH 7.4 (37 °C). (B) Three-dimensional structure of an ALP homodimer: two views of ALP dimer related by a 90° rotation (PDB, code "P19111"). (D) Two other views of an ALP homodimer, related by a 180° rotation, showing the distribution of the superimposed residues, Glu (in blue) and Asp (in red) amino acids. Figures and sizes were generated using RasMol (v.2.7.5.2). (E and F) Measurements of the catalytic activity of ALP in aqueous solution (CaCl₂ = 11.6 mM) under different conditions, as indicated. (E) Evolution of the catalytic activity (initial velocity) as a function of the enzyme concentration. (F) Specific activity of ALP under different conditions.

the d_H value and the maximum value was observed at the iep of ALP, owing to the extensive aggregation of the enzymes. In solution, each ALP dimer is surrounded by multiple water molecules interacting particularly with the polar and charged amino-acid residues of the protein through hydrogen bonds.^{40,41} Moreover, the water molecules trapped into the bulk of the enzyme contribute to loosen its macromolecular structure leading to an increase in its volume. The three-dimensional structure available in the protein data bank³⁹ provided helpful information about the size of the dimer and the visualization of the monomer/monomer interface (Fig. 1B). It showed the computed dimensions of $8.9 \times 5.8 \times 7.9 \text{ nm}^3$ for the dimer. The size measured by DLS at $\text{pH} \geq 6$ ($d_H \sim 20 \text{ nm}$, a negligible proportion of aggregates are observed in this range of pH) may be consistent with a tetrameric form.

Fig. 1C provides a comparison of DLS and ζ -potential data obtained in ALP solutions under three different physicochemical conditions: (i) pH 7.4 (RT) taken as the reference, (ii) pH 9 (RT), a pH value close to the optimum pH value for ALP activity,⁴² and (iii) pH 7.4 (37 °C), a physiologically relevant condition. The negatively charged surface of the enzyme is due to the presence of several tens of side chain $-\text{COOH}$ residues, originating from Glu (3.8%) and Asp (6.2%).³⁹ These residues are evenly distributed on the enzyme surface as clearly shown in the three-dimensional structure (see Glu in blue and Asp in red in Fig. 1D). At pH 9, ALP is more negatively charged than at pH 7.4 owing to a higher degree of deprotonation of the $-\text{COOH}$ and $-\text{NH}_3^+$ residues, originating from Lys and Arg. At pH 7.4 (37 °C), the ζ -potential value of ALP was also more negative than that at RT, which may be explained by a decrease in the pK_a value due to an increase in the Gibbs free energy with temperature.⁴³ It may be also associated with the changes in the protein conformation and/or its state of aggregation. Regarding DLS data, it appears that the enzymes maintain their three-dimensional structure, presumably in the form of tetramers, under the three studied conditions.

The activity of ALP under the studied conditions was also investigated. Fig. S1 (ESI†) shows the formation kinetics of pnp over time at different concentrations of ALP ranging from 1 to $100 \mu\text{g mL}^{-1}$. As expected, the concentration of pnp increased gradually with the concentration of ALP in the medium, fitting properly to the Michaelis–Menten model. In the first linear part of the curve corresponding to the initial activity of the enzyme, a noticeable, rapid increase was observed. Then, the slope of 4-nitrophenol (pnp) formation decreased with time owing to the decrease in the reaction kinetics. The initial activity as a function of the enzyme concentration is shown in Fig. 1E, indicating a linear relationship that provides the specific activity of ALP under the three studied conditions (Fig. 1F). It revealed the highest value at pH 9 (RT) which is close to the optimum pH value for ALP activity.

2.2 Assembly/mineralization on planar surfaces

The incorporation of active ALP enzymes into a multilayered film and subsequent mineralization are examined under the

three studied conditions: pH 7.4 (RT), pH 9 (RT) and pH 7.4 (37 °C). For this purpose, the sequential LbL assembly method was used. As can be seen from its three-dimensional structure, ALP exhibits the negatively-charged residues which are randomly distributed and accessible at the macromolecular surface (Fig. 1D). This may allow its adsorption onto its polycation counterpart, *e.g.* PAH, without a preferential orientation. The building and the subsequent mineralization of $(\text{PAH}/\text{ALP})_n$ multilayers (where n represents the number of adsorbed bilayers) were monitored *in situ* using a QCM-D. Typical shifts in the resonance frequency (Δf) and dissipation (ΔD) recorded at pH 7.4 (RT) during (i) the alternate adsorption of polyelectrolytes and enzymes, and (ii) subsequent mineralization are shown in Fig. 2A. Noticeable shifts in the frequency and dissipation were observed during each injection step of ALP into the QCM-D cell. The addition of PAH gave rise, however, to an increase in Δf and a decrease in ΔD suggesting either a partial desorption or a compaction of the multilayers (Fig. S2, ESI†). Similar behavior was observed in other proteins, such as denatured collagen,⁴⁴ and was attributed, in this case, to the formation of soluble protein–polyelectrolyte complexes. Similar multilayer growths were also observed at pH 9 (RT) and at pH 7.4 (37 °C) (Fig. S2, ESI†). The plots of $-\Delta f$ vs. n , explored to monitor the building of the multilayers as a function of the number of added bilayers, showed a clear saw-toothed pattern for all the studied conditions up to 5 bilayers, except that the increase of $-\Delta f$ was more pronounced at pH 7.4 (RT) (Fig. 2B). These findings demonstrated the successful incorporation of ALP into LbL assemblies under different physicochemical conditions.

Regarding mineralization, after the construction of $(\text{PAH}/\text{ALP})_5$ multilayers, a solution containing Ca^{2+} ions and α -glycerol phosphate was injected into the QCM-D cells at the same pH and temperature as the LbL growth conditions. At pH 7.4 (RT), a significant shift in the frequency towards negative values (around -1600 Hz) was observed with a strong increase of dissipation signal (Fig. 2A). This suggests the formation of mineralized structures on the surface. The injection of only either Ca^{2+} ions or α -glycerol phosphate did not induce any noticeable shifts in Δf and ΔD signals (Fig. S3, ESI†). This clearly indicates that both Ca^{2+} and α -glycerol phosphate, the substrate of the enzyme, are required for mineralization at the solid surface. At pH 9 (RT) and pH 7.4 (37 °C), the frequency shift was around 4 to 5 times lower than that at pH 7.4 (RT) (Fig. S2, ESI†), indicating less extensive mineralization compared to pH 7.4 (RT). The dissipation was also about 40 times lower than that at pH 7.4 (RT) and did not exceed 12×10^{-6} (Fig. S2, ESI†). Complementary insights into the growth mechanism of the mineralized layer is provided by the parametric plots of the ratio $\Delta D/-\Delta f$ as a function of $-\Delta f$ (Fig. 2C). The $\Delta D/-\Delta f$ ratio is proportional to the elastic compliance and thus gives a relative measure of the layer softness, whereas $-\Delta f$ gives a relative measure of the surface coverage.⁴⁵ This approach, initially developed to characterize monolayer systems, has been recently used to investigate multilayered films.⁴⁶ At pH 9 (RT) and pH 7.4 (37 °C), a decrease in the

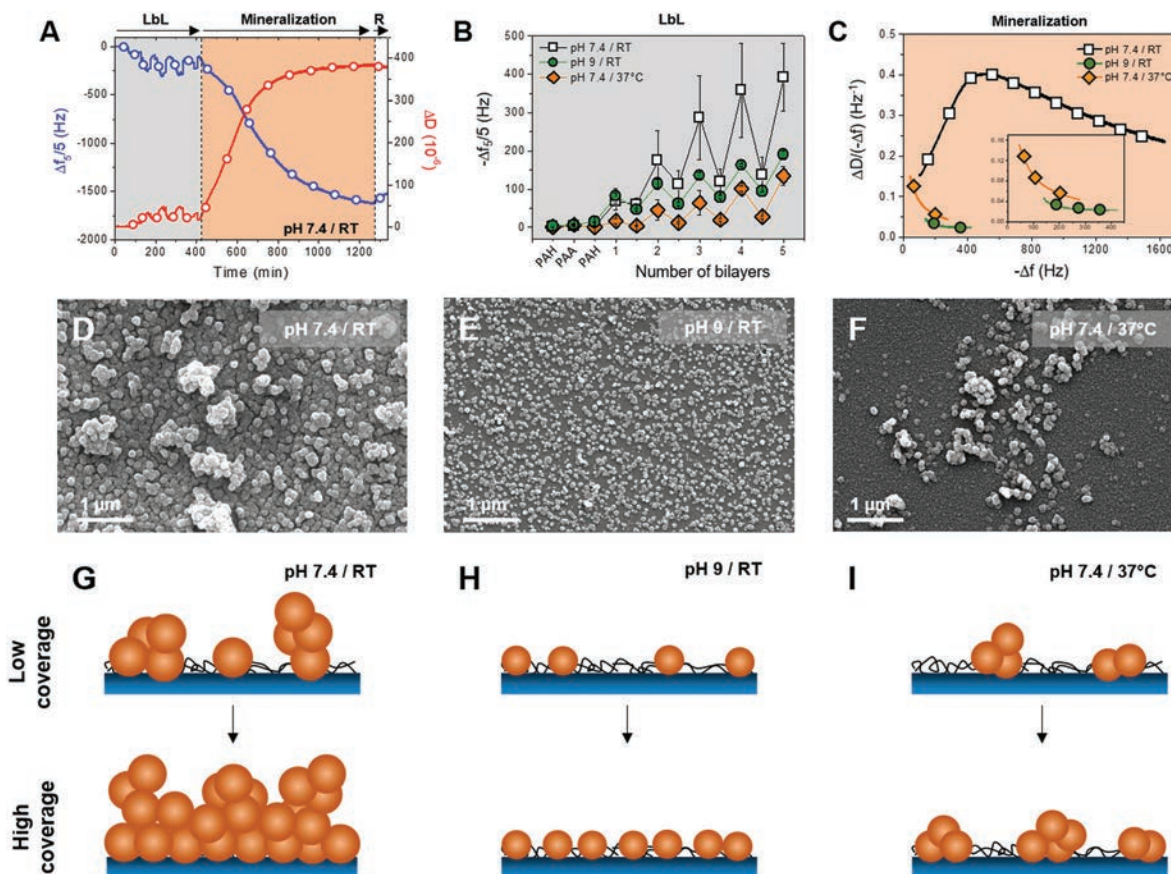


Fig. 2 Enzyme-assisted-mineralization on a planar surface. (A) QCM-D measurements showing the frequency changes in the 5th overtone and the corresponding dissipation during the (PAH/ALP)_n LbL assembly followed by the mineralization at pH 7.4 (RT) and rinsing (R), as indicated by the arrows on the top of the graph. (B) The frequency shift, taken at the 5th overtone, as a function of the number of bilayers *n*, upon building (PAH/ALP)_n under the studied conditions: pH 7.4 (RT), pH 9 (RT) and pH 7.4 (37 °C). (C) Typical changes in the $\Delta D/-\Delta f$ ratio as a function of $-\Delta f$ of the mineralization after the (PAH/ALP)_n LbL assembly under the same studied conditions. (D–F) SEM images recorded after building the (PAH/ALP)₅ bilayers and subsequent mineralization under different conditions, as indicated. (G–I) Sketch depicting the growth mechanisms of the mineral phase in the LbL film at an early stage (low coverage) and after 24 h (high coverage) of mineralization under different conditions, as indicated. For the sake of clarity, CaP compounds are presented as globular particles, the diameter of which varies in a proportion consistent with the sizes shown in SEM images.

$\Delta D/-\Delta f$ ratio with an increasing $-\Delta f$ was observed, indicating that the layer progressively stiffens due to the formation of mineralized structures. The situation at pH 7.4 (RT) is however different; the $\Delta D/-\Delta f$ vs. $-\Delta f$ plot exhibited two regimes. First, the ratio $\Delta D/-\Delta f$ increased markedly, and then it decreased progressively with increasing $-\Delta f$ but remained significantly higher than that under the former conditions. The first regime could not be attributed to the swelling of the multilayers due to the presence of Ca²⁺ or α -glycerol phosphate ions, as this behavior was not observed with the injection of one of these ions (data from Fig. S3, ESI[†]). At pH 7.4 (RT), the first regime may correspond to the nucleation and growth of a few particles, probably aggregated and heterogeneously distributed on the surface, resulting in a striking increase of the $\Delta D/-\Delta f$ ratio (see Fig. 2G, low coverage). The second regime is then associated with further mineralization, the possible formation of multilayers made from nanoparticle aggregates, which progressively stiffen the layer. The latter phenomenon may be

explained by the lateral growth of the layer resulting from the fact that adjacent mineralized objects are brought into contact with each other (Fig. 2G, high coverage). This is consistent with the SEM observations obtained after 24 h of mineralization (Fig. 2D). Under other conditions, the growth of the mineralized films mainly involves the formation of smaller amount of particles in a less aggregated state, resulting in a rapid increase in the surface coverage, as shown in Fig. 2H and I. This growth mechanism is consistent with the morphology of the film obtained after 24 h of mineralization, as shown in SEM images (Fig. 2E and F).

The above findings clearly show that the immobilization of enzymes on the planar surface, through the LbL assembly, allows the catalytic activity to be maintained, and leads to the formation of mineralized films in the presence of Ca²⁺. Moreover, combined together, QCM-D data and SEM images clearly show that the growth mechanism of the mineral phase, induced by embedded enzymes within the LbL film, strongly

depends on the physicochemical conditions, namely pH and temperature.

2.3 Assembly/mineralization in nanoporous templates

Based on the results obtained for assembly/mineralization on planar surfaces, the LbL assembly and subsequent mineralization were performed within the nanopores of the track-etched membrane (template) according to the procedure depicted in Scheme 1. These assemblies were characterized by dissolving the membrane and imaging the liberated (PAH/ALP)₅ nanostructures. TEM micrographs showed the formation of (PAH/ALP)₅ nanotubes using templates with pore sizes of 200 and 500 nm, regardless of the conditions (Fig. S4, ESI†). The hollow structure of these nano-objects can be distinguished in TEM micrographs as they exhibit a higher electronic density at their edges when observed in transmission mode (*e.g.* see Fig. S4A, ESI†). However, their dimensions, that is, their length and outside diameter, greatly fluctuate. In fact, because of the small number of bilayers ($n = 5$), the walls of the nanotubes are too thin to maintain the mechanical integrity of the whole structure after membrane dissolution. This results in their breakdown, twisting or flattening when collecting them. The enzymatic activity of (PAH/ALP)₅ nanotubes within the template was monitored (Fig. S5, ESI†), showing that the immobilized enzymes remain active, regardless of the pore size of the template.

After the construction of (PAH/ALP)₅ multilayers, the templates were incubated in a solution containing Ca²⁺ ions and α -glycerol phosphate for 2, 24 and 48 h. It is worth noting that prior to immersion in the mineralization medium, the multilayers potentially formed on the top and bottom surfaces of the membranes were removed to ensure better diffusion of ions (see more details in Fig. S5, ESI†). After the template dissolution, the obtained nanostructures were collected and observed using electron microscopes. When using the template with a pore size of 500 nm at pH 7.4 (RT), the formation of particles distributed all along the tubular structure was observed by TEM, especially after 24 and 48 h of mineralization, and the average size of the particles was about 37 nm (Fig. 3A–C). SEM images revealed that the obtained nanostructures, after 48 h, exhibited a smooth surface and, probably, a hollow structure that may be seen in the broken areas (Fig. 3D). At pH 9, the formation of mineralized nanostructures was more pronounced (Fig. 3E–G), leading to the formation of particles with larger size, about 155 nm, after 24 h (Fig. 3F) and the formation of a hollow structure with a continuous mineralized wall after 48 h (Fig. 3G). The chemical nature of these CaP nanostructures was confirmed by the elemental maps (using EDX in STEM mode) of Ca (the inset of Fig. 3G,) and P (not shown). SEM images showed a morphology similar to that observed at pH 7.4 (RT). When the mineralization was performed at pH 7.4 (37 °C), small CaP particles, *ca.* 57 nm, were formed after 2 h (Fig. 3I), and evolved after 24 and 48 h into well-defined tubular structures with a distinct wall of about 70 nm thickness (Fig. 3J and K). These nanotubes were significantly more stable than those described

under other conditions; their length is in the range of a few μm and may reach 10 μm (Fig. 3L). The measurement of the diameter of all the nanostructures obtained under the three studied conditions showed that mineralization leads to a narrow size distribution with an outside diameter close to the diameter of the template nanopore, *i.e.* around 500 nm (Fig. 3M–O). This trend was more obvious when the mineralization was performed at pH 7.4 (37 °C).

The situation was radically different when using the template with a pore size of 200 nm (Fig. 4). At pH 7.4 (RT), no mineral phase was observed and only (PAH/ALP)₅ nanotubes were visible in TEM images, regardless of the incubation time in the mineralization solution (Fig. 4A–D). This result is not expected as enzymes remain active in the nanoporous template (Fig. S6, ESI†). This may be due to the fact that the mineralization at pH 7.4 (RT) (see the growth mechanism described on the planar surface, Fig. 1D) yields large aggregated/agglomerated CaP particles which could be unfavorable in this confined medium. At pH 9 (RT), extensive mineralization was observed, leading to the formation of nanowires completely filled with mineral particles until clogging the pores, particularly after 48 h (Fig. 4E–H). This clearly creates diffusion constraints that result in the formation of non-mineralized areas (Fig. 4G). Finally, the mineralization at 37 °C (pH 7.4) led to the formation of hollow nanostructures after 24 h (Fig. 4J) and the formation of nanowires uniformly filled with mineral particles after 48 h (Fig. 4K). Interestingly, in the latter case, the mechanical stability of nanotubes was shown to be remarkably high with lengths exceeding 10 μm (Fig. 4L). The outside diameter of the mineralized nanostructures obtained under the different studied conditions showed a narrow size distribution, and was particularly monodisperse at pH 7.4 (37 °C) and pH 9 (RT) at about 200 nm. Indeed, the polydispersity index (PDI), computed from the Gaussian diameter distributions measured by TEM, is markedly higher at pH 7.4, RT (PDI = 0.45) than those computed under other studied conditions (PDI = 0.09 at pH 9 (RT) and PDI = 0.14 at pH 7.4 (37 °C)).

Particular attention is dedicated to the morphology and composition of the nanowires obtained at pH 7.4 (37 °C) after 48 h. Fig. 5A and B present higher magnification TEM micrographs and the corresponding elemental maps obtained by EDX for phosphorus, calcium, oxygen and nitrogen, respectively. They revealed the formation of well-defined nanowires filled with highly aggregated elongated nanostructures. Maps clearly showed that the nanowires are entirely composed of CaP compounds. The accumulation of nitrogen also indicates the presence of enzymes and the PAH polyelectrolyte used for the LbL assembly. Importantly, these nanowires are made of crystalline CaP, which was identified by SAED (Fig. 5C) and HRTEM (Fig. 5D). The SAED pattern revealed the crystallization of hydroxyapatite in the hexagonal lattice by the (002) and (112) diffraction spots (Fig. 5C). The inter-reticular distances of the obtained calcium phosphate were evaluated using the line intensity profiles extracted from HRTEM micrographs, thus confirming the crystalline lattice planes of hydroxyapatite with a d -spacing of $d_{002} = 3.4 \text{ \AA}$ (Fig. 5D). TEM micrographs, in

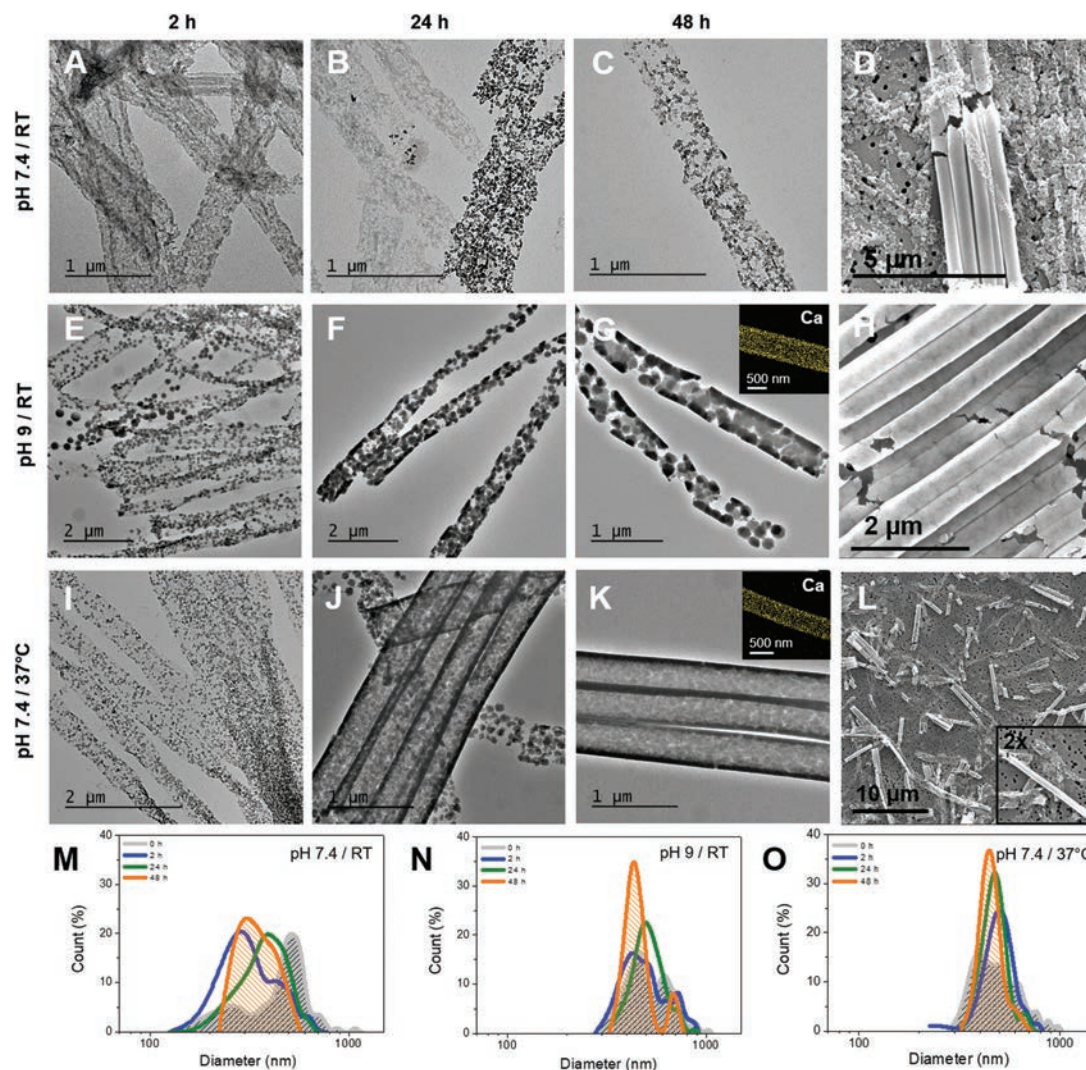


Fig. 3 Enzyme-assisted mineralization in nanopores (500 nm pore size template). TEM micrographs of the (PAH/ALP)₅ nano-objects after mineralization for 2 h, 24 h, and 48 h at (A–C) pH 7.4 (RT), (E–G) pH 9 (RT) and (I–K) pH 7.4 (37 °C), respectively, with the elemental map of calcium (G and K, inset); (D, H and L) SEM images of the (PAH/ALP)₅ nano-objects mineralized for 48 h at pH 7.4 (RT), pH 9 (RT) and pH 7.4 (37 °C) respectively; (M–O) size distributions (100 nano-objects) of the diameter of the nanotubes prior to (0 h) and after mineralization for 2 h, 24 h, and 48 h (as indicated) at pH 7.4 (RT), pH 9 (RT) and pH 7.4 (37 °C) respectively.

combination with the SAED pattern, thus revealed that the mineral phase is mainly hydroxyapatite with a typical platelet-like structure (see Fig. S7, ESI[†] for more details), which is similar to those observed using an enzyme-assisted mineralization process in homogeneous phase.³⁷ Only the side view of the platelets is clearly observed, whereas it is difficult to visualize their basal plane, suggesting that they are highly stacked within the nanowire (Fig. S7, ESI[†]). The morphology of the latter nanowires is in contrast with those obtained in the 500 nm pore size template under the same conditions, showing a clear hollow structure and a wall with a thickness of about 70 nm (Fig. 5E). Moreover, they are made of amorphous CaP as characterized by the absence of diffraction spots in the SAED pattern (not shown).

The above findings showed that the template pore size plays a pivotal role in the mineralization process, particularly

regarding the morphology and crystallinity of CaP compounds and the mechanical stability of the obtained nano-objects. To thoroughly examine this hypothesis, complementary enzyme-assisted mineralization experiments were performed in the template with a pore size of about 300 nm under conditions at which the formation of crystalline hydroxyapatite was observed, *i.e.* at pH 7.4 (37 °C). Interestingly, both nanowires densely filled with crystalline platelets (Fig. 5F) and hollow nanotubes made of amorphous particles (Fig. 5D) were obtained. However, all of the observed nanostructures were either purely crystalline or purely amorphous. A rough estimate of the proportion of amorphous/crystalline nanostructures may be provided, the distinction being made based on their morphologies as clearly shown in Fig. 5F and G. The results showed a noticeable increase in the fraction of amorphous nanostructures with an increase in the template pore

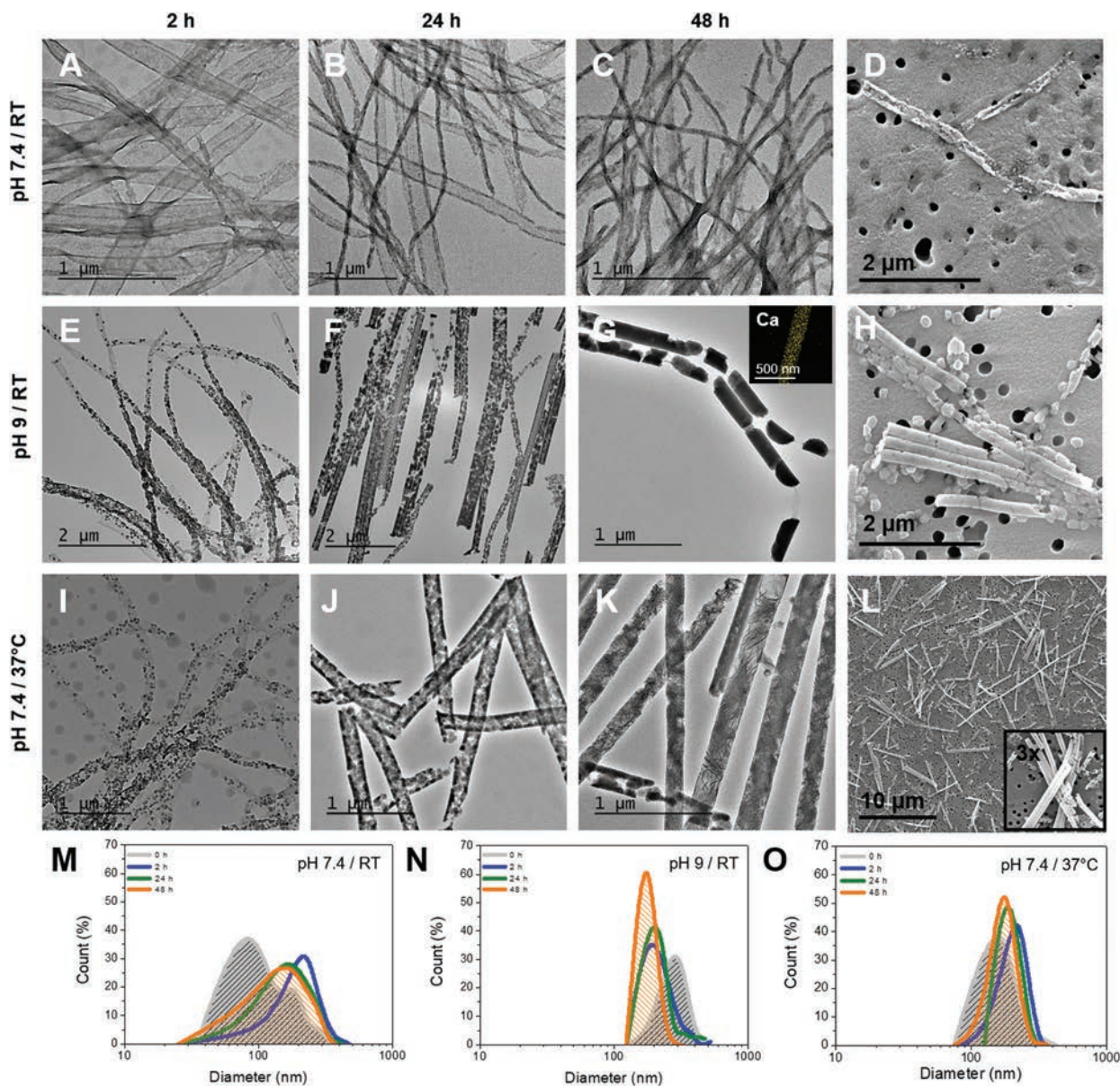


Fig. 4 Enzyme-assisted mineralization in nanopores (200 nm pore size template). TEM micrographs of the (PAH/ALP)₅ nano-objects after mineralization for 2 h, 24 h, and 48 h at (A–C) pH 7.4 (RT), (E–G) pH 9 (RT) and (I–K) pH 7.4 (37 °C), respectively, with the elemental map of calcium (G, inset); (D, H and L) SEM images of the (PAH/ALP)₅ nano-objects mineralized for 48 h at pH 7.4 (RT), pH 9 (RT) and pH 7.4 (37 °C), respectively; (M–O) size distributions (100 nano-objects) of the diameter of the nanotubes/nanowires prior to (0 h) and after mineralization for 2 h, 24 h, and 48 h (as indicated) at pH 7.4 (RT), pH 9 (RT) and pH 7.4 (37 °C), respectively.

size (Fig. 5H). The aspect ratio, computed as the ratio of the mean diameter to the mean length of the mineralized nanostructures, followed an opposite trend; that is, it decreased with an increase in the pore size of the template (Fig. 5H). These observations provide relevant information regarding the mechanical stability of the mineralized nanostructures, suggesting that the nanostructures containing crystalline platelets exhibit a better mechanical stability than the amorphous ones.

Following the procedure that led to the formation of crystalline platelet-containing nanostructures, the LbL assembly and

mineralization of (PAH/ALP)₅ multilayers were carried out within the track-etched membranes displaying a network of intersecting nanopores of 300 nm diameter (Fig. 6A). After dissolution of the templating membrane, highly-ordered interfaces made of intersecting nanowires were reproducibly obtained (Fig. 6B). Each tubular building block was filled with densely-aggregated CaP platelets (Fig. 6C).

These findings show the possible design of a self-supported mineralized framework that may be easily fabricated and used in broad cell culture tests, such as to evaluate the differentiation process of mesenchymal stem cells. Interestingly,

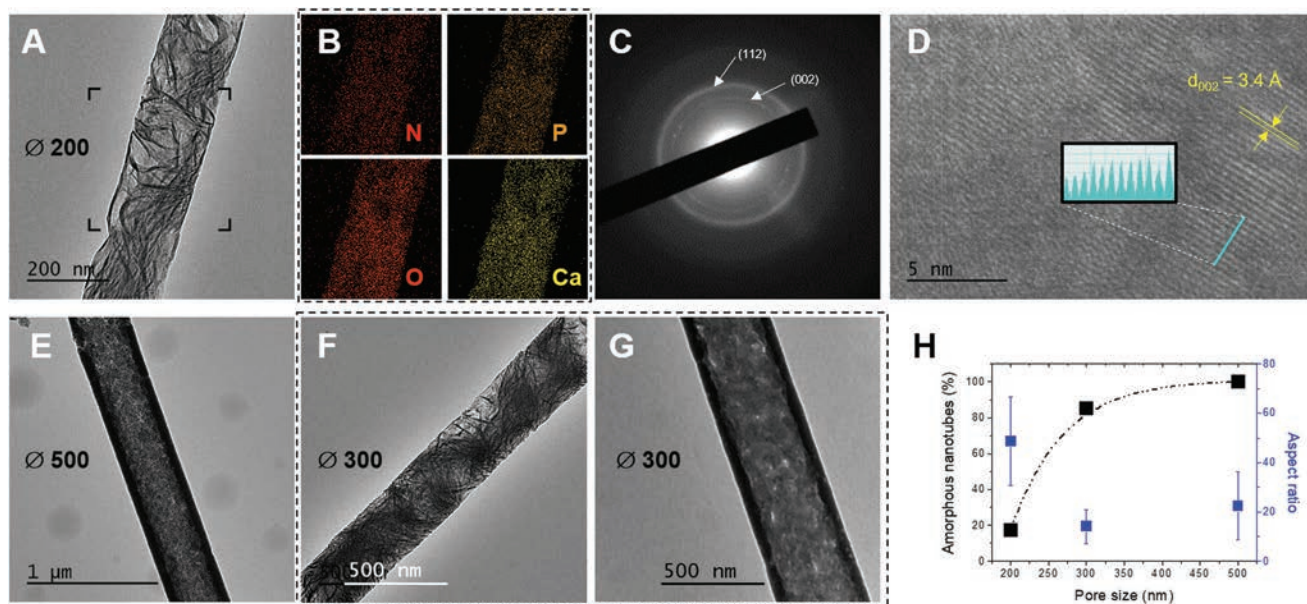


Fig. 5 (A) TEM micrograph focused on a platelet-containing nanowire synthesized at pH 7.4 (37 °C) for 48 h in the 200 nm pore size template with (B) the corresponding elemental maps of nitrogen, oxygen, phosphorus and calcium. (C) SAED pattern and (D) HRTEM micrograph showing inter-reticular distance from the line profile. (E) Typical micrographs of mineralized nanotubes/nanowires at pH 7.4 (37 °C) for 48 h using a template with a mean pore diameter of (E) 500 or (F and G) 300 nm, as indicated. (H) Proportion of amorphous nanotubes/nanowires (100 nano-objects) and the aspect ratio measured for each sample as a function of the pore size.

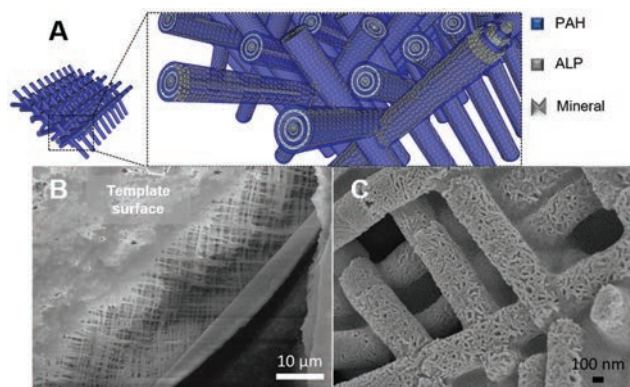


Fig. 6 Enzyme-assisted mineralized network of intersecting (PAH/ALP)₅ nanowires: (A) schematic illustration. (B and C) SEM images at increasing magnification of the template-free mineralized interfaces: (B) lateral view of the networks, showing the numerous intersections between the nanowires, giving rise to a nanostructured network; (C) high magnification of the network edge, showing the lamellar structure of intersecting nanowires, the characteristic of the enzyme-assisted mineralization process of CaP crystals.

owing to the versatility of the LbL technique, the range of achievable bioactivities can be considerably extended to integrate additional substances originally delivered to the cells by the ECM (*e.g.* growth factors).

2.4 Crystallization in a confined medium

Several investigations focused on the effect of confinement on the mineralization of inorganic compounds by means of a

nanoporous template,^{47,48} a crossed-cylinder apparatus^{49–51} or a picoliter droplet.⁵² It has been shown in particular that confinement has a significant impact on the crystallization of minerals. In the most general trend, it has been observed that a confined medium stabilizes the amorphous phase of CaP. However, the nature of physicochemical processes influenced by confinement remains unclear (diffusion of ions, adsorption, nucleation, crystallization, dissolution, *etc.*). Importantly, confinement is a parameter that could not be exclusively considered, independently of the chemical environment in which the mineralization is initiated. In contrast to the results described in the literature (see above), herein, the mineralization is induced locally through immobilized enzymes, *i.e.* via a heterogeneous catalytic reaction, in the presence of a polyelectrolyte, PAH, which may in turn influence the crystallization process. Polyelectrolytes may, indeed, influence the CaP crystallization process both in the homogeneous phase^{53,54} and in multilayered films.^{55–57} It is thus crucial to decipher, in the present study, the role of the polyelectrolyte used, particularly when CaP nucleation and growth presumably occur at the solid/liquid interface. For this purpose, a series of enzyme-induced mineralization tests were carried out both in solution and in the adsorbed phase (on a planar surface), and characterization performed in a manner to reliably discriminate the amorphous *vs.* crystalline CaP phases. In solution (homogeneous phase), well-crystallized platelet-shaped hydroxyapatite particles were obtained at pH 7.4 both at RT (Fig. 7A) and at 37 °C (Fig. 7D) after 48 h of mineralization. SAED patterns clearly show bright diffraction rings which are the (002) and the (112) diffraction of hydroxyapatite (Fig. 7B and E). IR

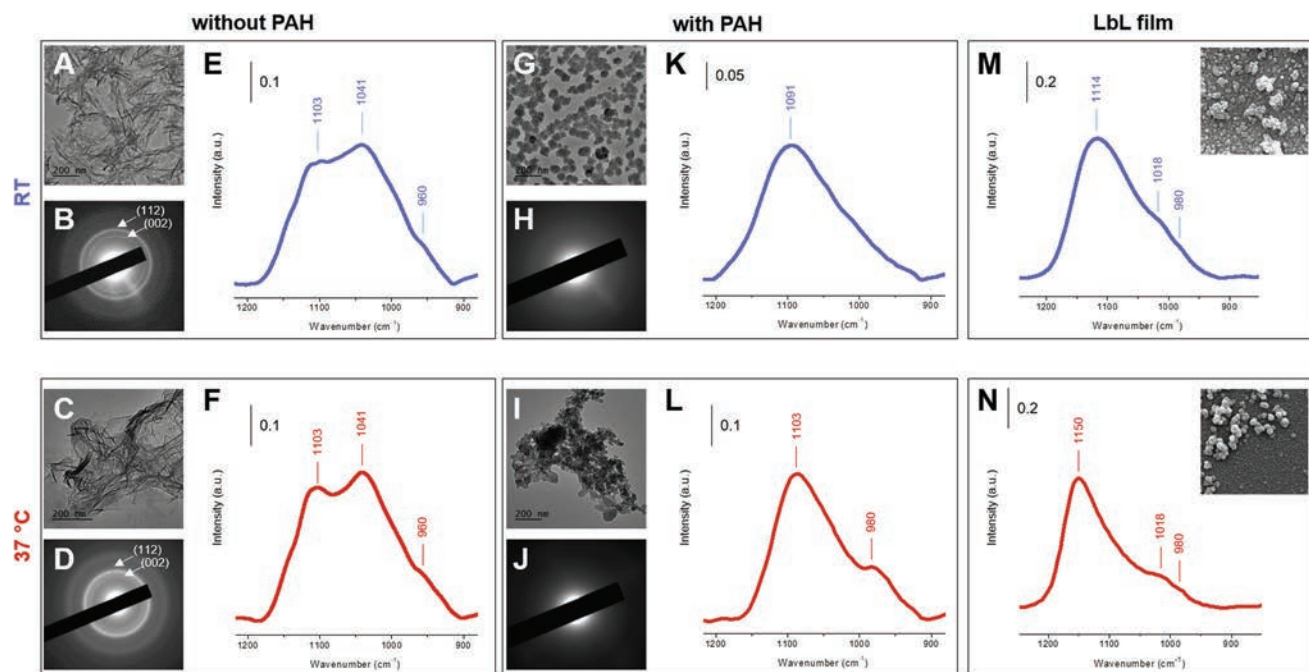


Fig. 7 Morphologies, crystallinity, and vibrational characteristics of calcium phosphate compounds formed in the presence of PAH in solution (homogeneous phase) or in the adsorbed state (heterogeneous phase) at RT or 37 °C, as indicated. (A, D, G and J) TEM micrographs, (B, E, H and K) SAED patterns and (C, F, I and L) PM-IRRAS spectra recorded on CaP particles formed in aqueous solution (pH 7.4) without (C–F) or with (I–L) the addition of PAH (1 mg mL⁻¹). (M and N) PM-IRRAS spectra recorded after building the (PAH/ALP)₅ bilayers and subsequent mineralization at pH 7.4 at (M) RT or (N) 37 °C.

analysis showed almost identical vibrational fingerprints in the 900–1200 cm⁻¹ region due to $\nu_3(\text{PO}_4^{3-})$ and $\nu_1(\text{PO}_4^{3-})$ (Fig. 7C and F). In contrast, in the presence of PAH in solution, the mineralization of calcium phosphate was strongly affected and resulted in the formation of globular (Fig. 7G and J) and amorphous structures, as shown by the diffusive diffraction results (Fig. 7H and K). IR spectra showed a noticeable change in the spectrum shape which leads to a striking decrease of the band at about 1041 cm⁻¹ (Fig. 7I and L). The stabilization of the amorphous phase in the presence of PAH is consistent with previous findings.⁵⁸ The effects of different polyelectrolytes, anionic or cationic, on the mineralization of inorganic compounds has been, indeed, widely investigated in solution.^{48,58–62} It has been suggested that polyelectrolytes are adsorbed onto the surface of the amorphous calcium phosphate particles, and prevent further interaction with the calcium and phosphate ions, which limits their crystallization.^{58,59,61} This is what is observed, for instance, for poly(ethylene imine).⁵⁹

In the adsorbed phase (LbL film), IR data showed a fingerprint similar to that observed previously in PAH solution (Fig. 7M and N). This suggests the formation of poorly crystalline/amorphous CaP compounds with a globular shape on the planar surface as observed in SEM images (see the insets of Fig. 7M and N). Furthermore, the same trend was observed at RT and at 37 °C. Accordingly, on planar surfaces, the mineralization through immobilized enzymes, embedded within the polyelectrolyte multilayers, seems to lead to the formation of

poorly crystalline/amorphous CaP compounds, independently of the temperature. The main characteristics of all these CaP compounds obtained under the studied conditions (RT *vs.* 37 °C; with *vs.* without PAH) in solution, on planar surfaces or in nanopores are summarized in Table S1 (ESI†). It appears that temperature mainly impacts the growth mechanism of mineralized particles on the planar surface (see the mechanism depicted in Fig. 2G and I) but not the crystallinity.

In 500 nm diameter nanopores, the situation seems to be comparable to the planar surface; the nanopore wall may be, in this case, viewed as a planar surface at the length scale at which the mineral particles grow. In contrast, in nanopores with 200 nm diameter, a confinement effect is observed, impacting the crystallinity of the mineral phase. Importantly, the fact that the formation of highly crystalline platelets of hydroxyapatite was observed only at 37 °C, and not at RT, indicate that the confinement could not be limited to a “templating effect”, as observed elsewhere.⁶³ Indeed, while the temperature did not induce noticeable changes in the kinetics of the enzymatic reaction (see Fig. 1F), it may influence the diffusion of ions, the mechanism of nucleation and phase transformations. Thus, evidencing the precise mechanism in a confined medium would be an important result, the question clearly deserves further investigation.

The above findings support a synergetic effect in the process of enzyme-assisted calcium phosphate mineralization to produce a crystalline phase, hydroxyapatite. It mimics the process by which organisms exploit the extracellular space to

direct the crystallization process. This mainly includes the control of three key factors:

(i) chemical environment (polyelectrolyte multilayers) mimicking proteins from the extracellular matrix, but the study can also be extended to other macromolecules (proteins, polysaccharides, *etc.*) in the ECM,

(ii) *in situ* generation of CaP precursors (orthophosphate ions) through an enzyme-assisted process, mimicking matrix vesicles which are known to initiate mineralization enzymatically, and

(iii) confinement, using nanoporous templates, mimicking confined locations in the ECM where the mineralization process may be initiated, such as within collagen fibrils (*cf.* intrafibrillar mineralization).

From a material chemistry perspective, the biomimetic approach proposed in the present study may pave the way toward the design of crystalline nano-objects with highly ordered anisotropic features, which can be used in various biomedical applications.

3. Conclusion

In summary, combining the (i) LbL assembly, (ii) heterogeneous enzymatic catalysis and (iii) template-based method is a relevant way to control the mineralization process of calcium phosphate compounds. This study reveals that the *in situ* generation of orthophosphate ions through immobilized enzymes in a confined medium leads to the formation of highly crystalline hydroxyapatite. The approach described in this paper opens up new horizons for designing biomimetic functional scaffolds while tailoring their properties at the supramolecular level. Indeed, this may be achieved by combining an *in situ* generation of mineral precursors, through an enzyme-catalyzed reaction, and the use of a template with intersecting nanopores. The fine-tuning of a set of parameters including ALP, its substrate and Ca^{2+} ion concentration and mineralization time, pH and temperature is foreseen to modulate the properties of the three-dimensional structure, particularly the mechanical stability. Besides, the enzyme-assisted mineralization of hydroxyapatite/CaP nanocrystals/lamellae/nano-platelets directly inside such confined environments is expected to accurately mimic the mineralization processes naturally occurring *in vivo* within the ECM of some tissues. The synthesized ECM-like interfaces could therefore be of peculiar interest to any application requiring the mimicry of native tissue environment: tissue engineering, regenerative medicine, biosensing devices, drug delivery, *etc.*

4. Experimental section

4.1 Materials

Poly(allylamine hydrochloride) (PAH, $M_w \sim 17$ kDa), poly(acrylic acid) (PAA, $M_w \sim 15$ kDa), alkaline phosphatase from bovine intestinal mucosa (ALP, ≥ 10 U mg^{-1}), sodium chloride

(NaCl, $\geq 99\%$), calcium chloride (CaCl_2 , $\geq 99\%$), α -glycerol phosphate magnesium salt hydrate ($\sim 85\%$), 4-nitrophenyl phosphate disodium salt hexahydrate (pnpp, $\geq 99\%$) and 4-nitrophenol (pnp) were purchased from Sigma-Aldrich (France). Hydrochloric acid (HCl, 37%) was purchased from VWR (France) and 9.31 M sodium hydroxide (NaOH) was purchased from Volusol (US/Canada). Polyelectrolyte, ALP and mineralization solutions were prepared in ultrapure water (MilliQ, Millipore, France) and their pH values were adjusted by adding 0.1 M HCl or 0.1 M NaOH.

4.2 Mineralization in solution

A solution of CaCl_2 (11.4 mM) was prepared in ultrapure water. α -glycerol phosphate was then added to obtain the final concentration of 7 mM. ALP was subsequently added at the final concentration of 0.1 mg mL^{-1} . The solution was finally adjusted to pH 7.4 and the mixture was gently stirred for 48 h at RT, forming a precipitate. It was then centrifuged, washed three times with ultrapure water and dried under air. The procedure was also carried out at pH 9 (RT) and at pH 7.4 (37 °C).

4.3 Procedures on planar surfaces

Glass slides ($\varnothing = 10$ mm, VWR, France) were cleaned beforehand in piranha solution (30% H_2O_2 and 96% H_2SO_4 mixed in 1:3 ratio) for 20 min and then thoroughly rinsed with ultrapure water. The adsorption process was carried out under the three studied conditions: pH 7.4 (RT), pH 9 (RT) and pH 7.4 (37 °C), by first incubating the support in the PAH solution (1 mg mL^{-1}) and then in the PAA solution (1 mg mL^{-1}) for 10 min each to build an anchoring layer. The support was then alternately immersed in the PAH solution (1 mg mL^{-1}) for 10 min and in the ALP solution (0.1 mg mL^{-1}) for 30 min. Between each dipping step, the substrate underwent a rinsing step in two different water baths for 2 min each. After building 5 bilayers, the samples were incubated in the mineralization solution: 11.4 mM CaCl_2 and 7 mM α -glycerol phosphate magnesium salt hydrate at pH 7.4. The substrates were then rinsed in two different water baths for 2 min each and dried under nitrogen flow.

4.4 Procedures in nanoporous templates

The building of (PAH/ALP)₅ multilayers was performed under the three studied conditions: pH 7.4 (RT), pH 9 (RT) and pH 7.4 (37 °C), by immersing alternately a 25 μm thick polycarbonate (PC) membrane (1 cm \times 1 cm) with a pore size of 200 ($\varnothing = 204.9 \pm 14.4$ nm) or 500 nm ($\varnothing = 495.4 \pm 15.8$ nm) and a pore density of 1×10^8 pores per cm^2 supplied by It4ip (Louvain-la-Neuve, Belgium) in PAH (1 mg mL^{-1}) and ALP (0.1 mg mL^{-1}) solutions for 30 min each (Scheme 1). The membrane was rinsed in two water baths for 2 min each between each layer deposition. After the deposition of five PAH/ALP bilayers, the top and bottom surfaces of the membrane was decrusted with a cotton swab immersed in a solution of 3 M NaCl (pH 12) and then rinsed with water. The membrane was subsequently incubated in the mineralization solution at pH 7.4 (11.4 mM CaCl_2 and 7 mM α -glycerol phosphate magnesium salt

hydrate) for 2 h, 24 h and 48 h (Scheme 1). A rinsing step was then carried out in two different baths (2 min each) of water. The membrane was subsequently dried under nitrogen flow.

A similar procedure was used for building the (PAH/ALP)₅ multilayers within track-etched PC templates with a thickness of 25 μm, showing a network of 300 nm diameter nanopores intersecting at a controlled angle of ~90°, with a density of 2.8 × 10⁸ pores per cm² (supplied by It4ip).

4.5 DLS and ζ-potential

The solutions of ALP were studied by dynamic light scattering (DLS) and electrophoretic mobility (EPM) in water. In order to perform significant DLS measurements, the concentration of the enzyme dispersion was set at 1.0 mg mL⁻¹. The DLS correlograms were recorded using a Zetasizer Nano ZS instrument (Malvern, France). The General Purpose algorithm (non-negative least squares (NNLS) analysis) in the Zetasizer software was used to fit the measured correlograms. DLS is a technique that is used for measuring the intensity-weighted size distribution of particle dispersions. It is extremely sensitive even to very small quantities of aggregates, as the size distribution is proportional to the sixth power of the particle size. In order to give a more representative result, the hydrodynamic diameters reported herein correspond to the values of the intensity-weighted distribution peaks, taking into account their relative amount in extrapolated number-weighted distributions. Above ca. 1 μm the hydrodynamic diameters determined for this kind of system correspond to large aggregates for which the size cannot be very well defined.

ζ-Potential calculations through EPM measurements were carried out using a Malvern Zetasizer nano ZS equipped with disposable polystyrene cuvettes (DTS1061, Malvern Instruments Ltd, UK). The calibration of the instrument was performed using a ζ-potential transfer standard polystyrene latex solution (DTS1235, Malvern). The experiments were performed with ALP dispersions (100 μg mL⁻¹) and the obtained results correspond to the mean of five replicates.

4.6 A quartz crystal microbalance with dissipation monitoring (QCM-D)

The LbL assembly was monitored *in situ* using a QCM-D. Measurements were performed at RT (22 °C) or at 37 °C using a Q-Sense E4 System (Sweden). The adsorption of particles was performed onto sensors coated with a thin layer of SiO₂ in the Q-Sense system. The sensors were cleaned by UV-Ozone for 15 min and rinsed with ethanol before measurement. The oscillation of the quartz crystal at the resonant frequency (5 MHz) or at one of its overtones (15, 25, 35, 45, 55, and 65 MHz) was obtained by applying an ac voltage. The shifts in the resonance frequency (Δf) and dissipation (ΔD) were monitored upon adsorption of the different components. The reported results are based on the fifth overtone. Solutions were injected into the cells using a peristaltic pump (Ismatec IPC-N 4) at a flow rate of 50 μL min⁻¹. Prior to building the multilayers, water adjusted to pH 7.4 was used to establish the baseline. First, the PAH solution (1 mg mL⁻¹) adjusted to pH 7.4

was brought into the measurement cell for 10 min followed by a rinsing step with water at pH 7.4 for 10 min. The PAA solution (1 mg mL⁻¹) at pH 7.4 was then brought into the measurement cell for 10 min and rinsed for 10 min with water at pH 7.4. Then, PAH and ALP (0.1 mg mL⁻¹) solutions were alternately injected for 10 and 30 min, respectively. After building five bilayers, the cell was rinsed with water for 20 min and then the mineralization solution at pH 7.4 (CaCl₂ 11.4 mM and α-glycerol phosphate magnesium salt hydrate 7 mM) was injected into the cell overnight. The LbL assembly and mineralization were also performed under two additional conditions, pH 9 (RT) and pH 7.4 (37 °C), following the same procedure as described above.

4.7 Electron microscopies

Scanning electron microscopy (SEM). Mineralized multilayers were imaged using a scanning electron microscope (SEM, FEI Quanta FEC 250) at an acceleration voltage in the range of 10–20 kV. After rinsing in three water baths at pH 7.4 and subsequent drying under nitrogen gas, samples were metallized by gold sputtering for a better image contrast.

The morphology of nanotubes was characterized by SEM by dissolving the PC membrane in 3 mL of dichloromethane and filtering through a 23 μm-thick poly(ethylene terephthalate) (PET) membrane that had an average pore size of 200 nm (supplied by It4ip) to entrap the liberated nanotubes, then rinsing with dichloromethane and drying under vacuum (Scheme 1).

Transmission electron microscopy (TEM). TEM micrographs were acquired using a JEOL JEM-2100F instrument equipped with a CCD camera, at an acceleration voltage of 200 kV. The PC membrane with embedded nanotubes was dissolved in 3 mL of dichloromethane and the nanotubes were collected on a copper mesh grid coated with an amorphous carbon film. The elemental content of the nanotubes was determined by performing energy-dispersive X-ray spectroscopy (EDX) measurements in scanning transmission electron microscopy (STEM) mode and their crystallinity by selected area electron diffraction (SAED). For each representative TEM micrograph, SAED patterns were recorded to determine the crystallinity of the nano-objects and possibly identify the crystal phase.

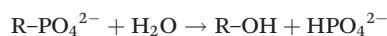
4.8 Polarization-modulation infrared reflection absorption spectroscopy (PM-IRRAS)

PM-IRRAS spectra were recorded on a commercial Nexus spectrometer (Thermo-Scientific, France). The external beam was focused on the sample with a mirror at an optimal incident angle of 80°. A ZnSe grid polarizer and a ZnSe photoelastic modulator, modulating the incident beam between p- and s-polarizations (PEM 90, modulation frequency = 37 kHz, Hinds Instruments, Hillsboro, OR), were placed in front of the sample. The light reflected from the sample was then focused onto a nitrogen-cooled mercury cadmium telluride (MCT) detector. All of the spectra presented were obtained from the sum of 128 scans; the band positions were estimated to have a resolution of 8 cm⁻¹. The samples were prepared as described in section 2.2 on glass substrates coated with a gold film. For

analyzing nanotubes, the PC membrane with embedded nanotubes was dissolved in 3 mL of dichloromethane and filtered through a PET membrane coated with a gold film to entrap the liberated nanotubes (Scheme 1). The PET membrane was then rinsed with dichloromethane and dried under vacuum.

4.9 Enzymatic assay

The enzyme activity was measured in solution by monitoring the production of pnp in the presence of a pnp substrate (7 mM) and CaCl₂ (11.4 mM), according to the following reaction:



where R is the nitrophenyl group.

The measurement was performed using a UV-visible spectrophotometer (Jenway 7315) at 410 nm as a function of time. The catalytic activity was monitored for “free” enzymes (in solution) and for membrane-embedded (PAH/ALP)₅ nanotubes under the three studied conditions: pH 7.4 (RT), pH 9 (RT) and pH 7.4 (37 °C). For the latter case a piece of PC membrane (5 × 5 mm²), incorporating (PAH/ALP)₅ multilayers, was placed in a 3 mL solution under gentle stirring.

Conflicts of interest

There are no conflicts to declare.

Acknowledgements

The authors thank Joanne Lê (LRS, Sorbonne University) for her technical assistance in enzymatic mineralization in the homogeneous phase, François Oudet, Frédéric Nadaut and Caroline Lefebvre (SAPC, UTC) for helping to perform TEM and SEM analyses, and Florence Billon (LISE, Sorbonne Université) for performing the gold-coating of track-etched membranes.

References

- 1 S. Ai, G. Lu, Q. He and J. Li, *J. Am. Chem. Soc.*, 2003, **125**, 11140–11141.
- 2 G. Lu, S. Ai and J. Li, *Langmuir*, 2005, **21**, 1679–1682.
- 3 S. Ai, Q. He, C. Tao, S. Zheng and J. Li, *Macromol. Rapid Commun.*, 2005, **26**, 1965–1969.
- 4 Y. Wang, A. S. Angelatos and F. Caruso, *Chem. Mater.*, 2008, **20**, 848–858.
- 5 Y. He and K. Park, *Mol. Pharmaceutics*, 2016, **13**, 2164–2171.
- 6 S. Hou, J. Wang and C. R. Martin, *Nano Lett.*, 2005, **5**, 231–234.
- 7 E. Ferain and R. Legras, *Nucl. Instrum. Methods Phys. Res., Sect. B*, 2003, **208**, 115–122.
- 8 K. Ariga, M. McShane, Y. M. Lvov, Q. Ji and J. P. Hill, *Expert Opin. Drug Delivery*, 2011, **8**, 633–644.
- 9 J. Landoulsi, C. J. Roy, C. Dupont-Gillain and S. Demoustier-Champagne, *Biomacromolecules*, 2009, **10**, 1021–1024.
- 10 J. Zhang, B. Senger, D. Vautier, C. Picart, P. Schaaf, J.-C. Voegel and P. Lavalle, *Biomaterials*, 2005, **26**, 3353–3361.
- 11 J. Hodak, R. Etchenique, E. J. Calvo, K. Singhal and P. N. Bartlett, *Langmuir*, 1997, **13**, 2708–2716.
- 12 M. Onda, Y. Lvov, K. Ariga and T. Kunitake, *Biotechnol. Bioeng.*, 1996, **51**, 163–167.
- 13 P. Quantin, E. Colaço, K. El Kirat, C. Egles, H. FICHEUX and J. Landoulsi, *ACS Omega*, 2018, **3**, 12535–12544.
- 14 Y. Lvov, H. Haas, G. Decher, H. Moehwald, A. Mikhailov, B. Mtchedlishvily, E. Morgunova and B. Vainshtein, *Langmuir*, 1994, **10**, 4232–4236.
- 15 J. M. Silva, R. L. Reis and J. F. Mano, *Small*, 2016, **12**, 4308–4342.
- 16 J. J. Richardson, J. Cui, M. Björnalm, J. A. Braunger, H. Ejima and F. Caruso, *Chem. Rev.*, 2016, **116**, 14828–14867.
- 17 S. Zhang, S. Demoustier-Champagne and A. M. Jonas, *Biomacromolecules*, 2015, **16**, 2382–2393.
- 18 D. M. Kalaskar, S. Demoustier-Champagne and C. C. Dupont-Gillain, *Colloids Surf., B*, 2013, **111**, 134–141.
- 19 D. G. Ramírez-Wong, S. Saghadzadeh, S. Van Herck, B. G. De Geest, A. M. Jonas and S. Demoustier-Champagne, *Biomacromolecules*, 2017, **18**, 4299–4306.
- 20 T. Komatsu, H. Terada and N. Kobayashi, *Chem. – Eur. J.*, 2011, **17**, 1849–1854.
- 21 T. Komatsu, *Nanoscale*, 2012, **4**, 1910–1918.
- 22 T. Komatsu, T. Sato and C. Boettcher, *Chem. – Asian J.*, 2012, **7**, 201–206.
- 23 C. J. Roy, L. Leprince, A. De Boulard, J. Landoulsi, V. Callegari, A. M. Jonas and S. Demoustier-Champagne, *Electrochim. Acta*, 2011, **56**, 3641–3648.
- 24 D. Lefèvre, J. Louvegny, M. Naudin, E. Ferain, C. Dupont-Gillain and S. Demoustier-Champagne, *RSC Adv.*, 2018, **8**, 22932–22943.
- 25 Y. Liu, S. Liu, D. Luo, Z. Xue, X. Yang, L. Gu, Y. Zhou and T. Wang, *Adv. Mater.*, 2016, **28**, 8740–8748.
- 26 H. Zhou and J. Lee, *Acta Biomater.*, 2011, **7**, 2769–2781.
- 27 N. J. Shah, J. Hong, Md. N. Hyder and P. T. Hammond, *Adv. Mater.*, 2012, **24**, 1445–1450.
- 28 Q. Hu, Z. Tan, Y. Liu, J. Tao, Y. Cai, M. Zhang, H. Pan, X. Xu and R. Tang, *J. Mater. Chem.*, 2007, **17**, 4690–4698.
- 29 N. Reznikov, M. Bilton, L. Lari, M. M. Stevens and R. Kröger, *Science*, 2018, **360**, eaao2189.
- 30 E. E. Golub, *Biochim. Biophys. Acta, Gen. Subj.*, 2009, **1790**, 1592–1598.
- 31 N. Rauner, M. Meuris, M. Zoric and J. C. Tiller, *Nature*, 2017, **543**, 407.
- 32 S. K. Samal, M. Dash, H. A. Declercq, T. Gheysens, J. Dendooven, P. V. D. Voort, R. Cornelissen, P. Dubruel and D. L. Kaplan, *Macromol. Biosci.*, 2014, **14**, 991–1003.
- 33 T. E. L. Douglas, P. B. Messersmith, S. Chasan, A. G. Mikos, E. L. W. de Mulder, G. Dickson, D. Schaubroeck, L. Balcaen,

- F. Vanhaecke, P. Dubruel, J. A. Jansen and S. C. G. Leeuwenburgh, *Macromol. Biosci.*, 2012, **12**, 1077–1089.
- 34 A. Aminian, K. Pardun, E. Volkmann, G. Li Destri, G. Marletta, L. Treccani and K. Rezwan, *Acta Biomater.*, 2015, **13**, 335–343.
- 35 M. Michel, Y. Arntz, G. Fleith, J. Toquant, Y. Haikel, J.-C. Voegel, P. Schaaf and V. Ball, *Langmuir*, 2006, **22**, 2358–2364.
- 36 Y.-Y. Jiang, Z.-F. Zhou, Y.-J. Zhu, F.-F. Chen, B.-Q. Lu, W.-T. Cao, Y.-G. Zhang, Z.-D. Cai and F. Chen, *Small*, 2018, **14**, 1804321.
- 37 E. Colaço, D. Brouri, C. Méthivier, L. Valentin, F. Oudet, K. El Kirat, C. Guibert and J. Landoulsi, *J. Colloid Interface Sci.*, 2020, **565**, 43–54.
- 38 M. Fosset, D. Chappelet-Tordo and M. Lazdunski, *Biochemistry*, 1974, **13**, 1783–1788.
- 39 <http://us.expasy.org>.
- 40 K. Haider, L. Wickstrom, S. Ramsey, M. K. Gilson and T. Kurtzman, *J. Phys. Chem. B*, 2016, **120**, 8743–8756.
- 41 A. C. Fogarty and D. Laage, *J. Phys. Chem. B*, 2014, **118**, 7715–7729.
- 42 Z. Yang, X.-J. Liu, C. Chen and P. J. Halling, *Biochim. Biophys. Acta, Proteins Proteomics*, 2010, **1804**, 821–828.
- 43 V. K. Rajan and K. Muraleedharan, *Int. J. Greenhouse Gas Control*, 2017, **58**, 62–70.
- 44 J. Landoulsi, S. Demoustier-Champagne and C. Dupont-Gillain, *Soft Matter*, 2011, **7**, 3337.
- 45 I. Reviakine, D. Johannsmann and R. P. Richter, *Anal. Chem.*, 2011, **83**, 8838–8848.
- 46 E. Colaço, D. Brouri, N. Aissaoui, P. Cornette, V. Dupres, R. F. Domingos, J.-F. Lambert, E. Maisonhaute, K. E. Kirat and J. Landoulsi, *Biomacromolecules*, 2019, **20**, 4522–4534.
- 47 B. Cantaert, E. Beniash and F. C. Meldrum, *Chemistry*, 2013, **19**, 14918–14924.
- 48 B. Cantaert, E. Beniash and F. C. Meldrum, *J. Mater. Chem. B*, 2013, **1**, 6586.
- 49 Y.-W. Wang, H. K. Christenson and F. C. Meldrum, *Chem. Mater.*, 2014, **26**, 5830–5838.
- 50 C. J. Stephens, S. F. Ladden, F. C. Meldrum and H. K. Christenson, *Adv. Funct. Mater.*, 2010, **20**, 2108–2115.
- 51 Y.-W. Wang, H. K. Christenson and F. C. Meldrum, *Adv. Funct. Mater.*, 2013, **23**, 5615–5623.
- 52 C. J. Stephens, Y.-Y. Kim, S. D. Evans, F. C. Meldrum and H. K. Christenson, *J. Am. Chem. Soc.*, 2011, **133**, 5210–5213.
- 53 A. Shkilnyy, A. Friedrich, B. Tiersch, S. Schöne, M. Fechner, J. Koetz, C.-W. Schlöpfer and A. Taubert, *Langmuir*, 2008, **24**, 2102–2109.
- 54 P. B.-Y. Ofir, R. Govrin-Lippman, N. Garti and H. Füredi-Milhofer, *Cryst. Growth Des.*, 2004, **4**, 177–183.
- 55 K. Abdelkebir, S. Morin-Grognon, F. Gaudière, G. Coquerel, B. Labat, H. Atmani and G. Ladam, *Acta Biomater.*, 2012, **8**, 3419–3428.
- 56 V. Ball, M. Michel, F. Boulmedais, J. Hemmerle, Y. Haikel, P. Schaaf and J. C. Voegel, *Cryst. Growth Des.*, 2006, **6**, 327–334.
- 57 P. A. Ngankam, Ph. Lavallo, L. Szyk, G. Decher, P. Schaaf and F. J. G. Cuisinier, *J. Am. Chem. Soc.*, 2000, **122**, 8998–9005.
- 58 P. B.-Y. Ofir, R. Govrin-Lippman, N. Garti and H. Füredi-Milhofer, *Cryst. Growth Des.*, 2004, **4**, 177–183.
- 59 A. Shkilnyy, A. Friedrich, B. Tiersch, S. Schöne, M. Fechner, J. Koetz, C.-W. Schlöpfer and A. Taubert, *Langmuir*, 2008, **24**, 2102–2109.
- 60 B. Cantaert, Y.-Y. Kim, H. Ludwig, F. Nudelman, N. A. J. M. Sommerdijk and F. C. Meldrum, *Adv. Funct. Mater.*, 2012, **22**, 907–915.
- 61 R. J. Coleman, K. S. Jack, S. Perrier and L. Grøndahl, *Cryst. Growth Des.*, 2013, **13**, 4252–4259.
- 62 J. M. Marentette, J. Norwig, E. Stockelmann, W. H. Meyer and G. Wegner, *Adv. Mater.*, 1997, **9**, 647–651.
- 63 D. Kim, B. Lee, S. Thomopoulos and Y.-S. Jun, *Nat. Commun.*, 2018, **9**, 962.